Video Article

Emission Spectroscopic Boundary Layer Investigation during Ablative Material Testing in Plasmatron

Bernd Helber[1,2], Olivier Chazot[1], Annick Hubin[2], Thierry E. Magin[1]

[1]Aeronautics and Aerospace Department, von Karman Institute for Fluid Dynamics

[2]Research Group Electrochemical and Surface Engineering, Vrije Universiteit Brussel

Correspondence to: Bernd Helber at helber@vki.ac.be

Abstract

Ablative Thermal Protection Systems (TPS) allowed the first humans to safely return to Earth from the moon and are still considered as the only solution for future high-speed reentry missions. But despite the advancements made since Apollo, heat flux prediction remains an imperfect science and engineers resort to safety factors to determine the TPS thickness. This goes at the expense of embarked payload, hampering, for example, sample return missions.

Ground testing in plasma wind-tunnels is currently the only affordable possibility for both material qualification and validation of material response codes. The subsonic 1.2MW Inductively Coupled Plasmatron facility at the von Karman Institute for Fluid Dynamics is able to reproduce a wide range of reentry environments. This protocol describes a procedure for the study of the gas/surface interaction on ablative materials in high enthalpy flows and presents sample results of a non-pyrolyzing, ablating carbon fiber precursor. With this publication, the authors envisage the definition of a standard procedure, facilitating comparison with other laboratories and contributing to ongoing efforts to improve heat shield reliability and reduce design uncertainties.

The described core techniques are non-intrusive methods to track the material recession with a high-speed camera along with the chemistry in the reactive boundary layer, probed by emission spectroscopy. Although optical emission spectroscopy is limited to line-of-sight measurements and is further constrained to electronically excited atoms and molecules, its simplicity and broad applicability still make it the technique of choice for analysis of the reactive boundary layer. Recession of the ablating sample further requires that the distance of the measurement location with respect to the surface is known at all times during the experiment. Calibration of the optical system of the applied three spectrometers allowed quantitative comparison. At the fiber scale, results from a post-test microscopy analysis are presented.

Video Link

The video component of this article can be found at http://www.jove.com/video/53742/

Introduction

On 6 August 2012, NASA's Mars Science Laboratory (MSL) mission successfully landed a rover on the Martian surface. This rover already includes an automated sample collection system for chemistry and mineralogy analysis. Not long after, on 12 November 2014, the robotic European Space Agency lander Philae achieved the first soft landing on a comet. These examples indicate that the next steps will be to identify, develop, and qualify required technologies for returning Martian or asteroid samples safely to Earth. Currently, ablative materials are the only option for the Thermal Protection System (TPS) of such sample return missions, which shields the spacecraft from the severe heating during hypervelocity entry. Chemical and physical decomposition of ablators transform the thermal energy into mass loss and recession, whilst the remaining solid material insulates the vehicle substructure[1,2]. With the methods presented throughout this protocol, we want to contribute with new experimental data to the ongoing efforts of improving the heat shield reliability by reducing design uncertainties and developing new thermo-chemical ablation models.

To achieve high performance characteristics of the ablative Thermal Protection Material (TPM) engineers of planetary probes and space vehicles make use of a wide range of composites[3,4]. TPMs are generally composed of a rigid precursor and a filling matrix, to serve as a pyrolyzing, ablating, and insulating material at low weight with reasonable mechanical properties. Current examples of a new family of porous lightweight ablators for high-speed entry missions, made of a carbon fiber preform impregnated with phenolic resin, are PICA (phenolic impregnated carbon ablator) developed by NASA[5,6], and the European ablator Asterm[7]. In addition to the space agencies in collaboration with industry, several research groups started on an academic level to manufacture and characterize new lightweight ablators, see for example references [2,8-12].

During atmospheric entry, part of the heat flux coming from the shock heated gas is transferred inside the heat shield and the virgin material is transformed following two mechanisms: Pyrolysis progressively carbonizes the phenolic resin into a low density, porous char, losing around

50% of its mass producing pyrolysis gases by vaporization. The pyrolysis gases are transported out of the material by diffusion and the pressure increase caused by their decomposition. They exhaust into the boundary layer, providing a further barrier for the heat exchange by blowing and undergo additional chemical reactions. The usage of polymers such as phenolic resins for the matrix takes advantage of their endothermic degradation nature, thereby absorbing energy, and serving as a binder for the other components. The second transformation phenomenon is the ablation of the char layer, composed of the carbonized resin and the remaining carbon fibers. This is promoted by heterogeneous chemical reactions, phase change and mechanical erosion, such as spallation, altogether leading to recession of the material.

Despite available flight data on the material performance during past missions, and efforts in material modeling[13,14], prediction of the heat flux to the spacecraft remains a critical problem. Ground testing in plasma wind-tunnels is currently the only affordable option for qualification of the thermal protection material. Additionally, new multi-scale material response models are proposed in order to take into account the porous micro-structure of the new class of materials[15,16]. Those models require extensive experimental data for their development and validation.

The facilities in use for material characterization are most commonly arc-heated[17-20] or induction coupled[21,22] torches, which provide high gas enthalpies with air as test gas, ideal for the simulation of atmospheric reentry. The subsonic 1.2MW Inductively Coupled Plasma (ICP) torch of the Plasmatron facility at the von Karman Institute (VKI) is able to reproduce the aerothermodynamic environment of atmospheric entry in the stagnation point boundary layer of a test object for a wide range of pressures and heat fluxes[23-25]. An extensive numerical rebuilding procedure offers a detailed characterization of the boundary layer and extrapolation of ground-test data to real re-entry flight conditions based on the Local Heat Transfer Simulation (LHTS) concept[26,27].

We present a procedure for material characterization on a porous carbon-fiber precursor in a well-characterized plasma gas environment representative of re-entry flight. The plasma freestream characterization is not part of this protocol but can be found elsewhere[28]. A comprehensive experimental setup of intrusive and non-intrusive techniques was integrated for *in-situ* analysis of the material exposed to the hot plasma flow. The results of those ablation experiments were already presented and widely discussed in another reference[28]. This protocol is meant to provide detailed information on the experimental techniques, their installation at the facility, and the procedures for data analysis. Target audiences of this publication are manifold: on the one hand, this publication is meant to provide a better insight into the experimental methods and procedures to improve the understanding of the facility's characteristics for material code developers and engineers of thermal protection materials. On the other hand, experimentalists of laboratories with similar facilities are addressed for data reproduction and comparison, and to extend the database of ablative material response to a wider heat-flux and pressure range.

Protocol

1. Facility Preparation

1. Define probe and sample-holder assignment based on availability and facility specifications (3 probe holders in this work) to obtain best views on test sample from outside the facility for optical measurements during the experiment.
2. If a pyrolyzing material is used, place the test sample in a cooled environment ($T < 200$ °C) prior to test start to prevent early degradation and outgassing.
3. Use available probe holders for heat flux measurements and pressure measurements of the plasma flow, details about heat flux and Pitot pressure measurements in the Plasmatron facility can be found in reference [24].

2. Measurement Techniques Setup

1. Emission spectrometer setup & alignment
   1. Identify the desired spectrometer depending on the test objectives and the available apparatus: Possible setups consist of several small, but broad spectral-range spectrometers for point measurements, or high-resolution spectrographs connected to a 2D CCD array allowing for spatially resolved measurements (for instance along the centerline or the radius of the plasma jet in front of the test samples).
   2. Depending on the chosen spectrometer configuration, determine the magnification that will be required and choose the appropriate lens as outlined below:
      1. Observe three locations within 4 mm (expected boundary layer thickness) in front of the test sample by the spectrometers, hence, 2 mm increments. This results in a magnification of $m = 3$ for the optical system due to the minimal distance between each of the fibers being limited to 6 mm by the fiber cladding (4 mm onto 12 mm yielding $m = 3$).
      2. Determine the required lens focal length by the magnification and thin lens equation:
      $m = s_i/s_o$, with s_i and s_o being the distances from the lens to the image and to the object, respectively; $1/s_o + 1/s_i = 1/f$, with f being the focal length of the lens.
      Note: In this protocol: $s_i = m \times s_o = 3 \times 1,000$ mm $= 3,000$ mm, resulting in $f = 750$ mm.
      3. Use mirrors if the distance between lens and object is impractically large (here 3,000 mm).
   3. Remove jacketing of the optical fibers in order to bring them as close together as possible and design a convenient mounting system. For example, use a simple press fit assembly with the fibers lying beside each other.
   4. Align the optical system (consisting of lens, mirrors, optical fiber ends) using a vertical and horizontal line laser: Bring all components to the same height (as the test sample) and align lens perpendicular to the sample's stagnation line (region in front of the sample's nose on the axis of the sample).
   5. Focus the optical path by placing the lens at distance s_o from the test sample and the optical fiber ends at distance s_i from the lens. Illuminate the sample stagnation point with a lamp and position the fiber ends at the location of the best focused image.
   Note: Creating the image of a pencil style Mercury calibration lamp positioned in front of the test sample can help: connect one spectrometer to an optical fiber and place the moveable fiber end where the strongest mercury emission occurs.

6. Once the lens-fiber system is aligned, send a laser point through the fiber ends (spectrometer side) and observe the focused laser on the sample side with a white paper sheet to confirm correct position and focusing in front of the test sample (prior to each test run).
7. Prevent any emission except that from the focal point from entering the optical fiber ends by enclosing the optical path with black cardboard. Crosscheck with a laser beam that no light except that focused by the lens and reflected by the mirrors reaches the fiber ends within the enclosed system. To do so, send a laser beam through the optical fibers (spectrometer side) and check that no light emitted by the fiber end is able to reach the lens directly.

2. High-Speed Camera (HSC)
    1. Use a high-speed camera for surface observation if available to allow for short exposure times for un-saturated images of the hot, ablating surface.
    2. Observe the test sample with the HSC perpendicular to the sample's surface. Use the sample - lens system axis for horizontal and vertical alignment of the camera optics. Make sure the center of field of view of the HSC coincides with the center of the lens and the sample stagnation point.
    3. Synchronize HSC and emission spectrometers with a Digital Delay Generator (DDG). Trigger the HSC recording with a single voltage peak from the DDG and trigger each spectrum recording with the desired frequency (2Hz) during the experiments (section 3).

3. Radiometry
    1. Use a two-color pyrometer for observation of the surface temperature in combination with a quartz window at the test chamber. Note: If very high target temperatures are expected, exceeding the measurement range of the device, consider decreasing the measureable radiance with an appropriate filter or window of lower transmittance.

3. Experimental Testing

1. Take photographs with a conventional DSLR camera, measure dimensions (using a caliber rule) and weight of the virgin test sample before installation in the test chamber.
2. Setup HSC software:
    1. Set high exposure time (90 msec) to align and focus the HSC prior to the experiment with the test sample in place and take a pre-test image (post-trigger = 1).
    2. Change exposure time for experiment (2-10 μsec), and set post-trigger to maximum (to store all frames), set correct recording rate (fps) to cover the full experiment (here 30-90 sec at 100 fps).
    3. Set initial f-number to f/16.
3. Set the DDG to the desired repetition rate at which spectra shall be recorded by the spectrometers (here: 2 Hz). The first trigger pulse will start the HSC acquisition.
4. Set up the spectrometer acquisition software (integration time τ_{exp}: depending on emission intensity, here: 20-150 msec, adapt during the experiment if necessary, average = 1).
    1. Make sure the optical system is still positioned correctly prior to the experiment with the sample in place (see step 2.1.6).
    2. Take background image S_{bg} with each spectrometer and save it.
    3. Change the trigger to 'external software', depending on the software (*e.g.*, SpectraSuite) (other options are: 'external', and 'synchronize', with different purposes).
    4. Save each spectrum when receiving a trigger pulse.
5. Install a high definition (HD) camera at any optical access if desired.
6. Place the test sample in the protection system and vacuum the test chamber using a group of three rotary-vane vacuum pumps and a roots pump.
7. Start the plasma facility and bring it to the desired test condition in terms of heat flux and pressure by adjusting the electric power input and the vacuum pumps. Use heat flux probe and the pitot probe (step 1.3) to observe the achieved conditions (1 MW/m^2 and 3 MW/m^2 at 15 hPa and 200 hPa).
8. Start recording of HD-camera and pyrometers.
9. Take a free-stream spectrum with all spectrometers available (for calibration comparison) then lower integration time to prevent saturation (from 200 msec to 50 msec).
10. Trigger HSC and spectrometers via DDG (see step 3.2 for setup) by pressing 'trig' and setting the mode from 'external' to 'internal'.
11. Inject the test sample into the plasma flow. Here, a pneumatic mechanism is used to inject the sample.
12. Adjust integration time of spectrometers if necessary to avoid saturation (ideally, any change of setup configuration should now be avoided).
13. Adjust aperture of HSC if necessary to prevent sensor saturation.
14. Remove test sample after desired test time (30 sec or 90 sec) into the sample protection system and shut down plasma flow.
15. Stop DDG and spectrometer acquisition, save HSC images, and stop pyrometer acquisition. Note: Leave pyrometer running if a material with high thermal capacity is tested to monitor cool-off phase (not necessary for CBCF preform).
16. Send laser point through optical fiber ends (spectrometer side) and observe laser focus with HSC, save this image to mark position of the spectrometer. Repeat this step with each spectrometer / optical fiber. ATTENTION: Make sure laser is not too strong to damage the CCD array of the camera. A discharging device is preferred. Alternatively, an image of the laser pointing on a paper sheet in front of the tested sample can be taken.
17. Place a chessboard at the position of the test sample and record image with HSC for calibration.
18. Remove test sample (*e.g.,* by hydraulic ejection), take weight, take photographs, and store in sample storage to protect the brittle char layer composed of oxidized fibers (do not touch the frontal sample surface).

4. Spectrometer Calibration

1. Spectral calibration
   1. Place a spectral calibration lamp in the focal point of the lens (*e.g.,* a pencil style Mercury lamp) to determine the wavelength calibration and the full-width-half-maximum (FWHM) of the optical system, details on those steps can be found in the literature[29].

2. Intensity calibration
   1. Perform an intensity calibration of each optical system consisting of the light collection mechanism (lens) and spectrometer efficiencies in $W/(m^2 \cdot sr \cdot nm)$ between 350 nm and 900 nm. Do this by placing a tungsten-ribbon lamp (OSRAM WI 17G) in the focus of each collection optic inside the test chamber. Record the calibration lamp's spectrum $S_{cal,\ exp}$ and obtain the calibration factor C by:
   $C = S_{cal,\ th} / (S_{cal,\ exp} - S_{bg,\ cal}) \times \tau_{cal}$,
   with the theoretical spectral response of the calibration lamp (provided by manufacturer) $S_{cal,\ th}$, the measured signal of the calibration lamp $S_{cal,\ exp}$, the background $S_{bg,\ cal}$, and the integration time during the calibration measurement τ_{cal}.

5. Data Processing

1. Surface recession rate and spectrometer probing location(s):
   1. Observe sample injection and ejection times on the HSC video file for correct test time estimation.
   2. Observe pixel location of the test sample stagnation point at injection from the HSC video file.
   3. Calibrate HSC magnification by exporting image taken in step 3.17 (for instance, .tiff format) and counting the pixels in the measurement region spanning multiple chessboard squares. Compute the correlation pixels:mm (obtain a more detailed characterization of the intrinsic and extrinsic camera parameters using the camera calibration toolbox in MATLAB if desired).
   4. Export the image(s) taken in step 3.16 (for instance, .tiff format) and find the pixels of the spectrometer probing location(s) as bright spots on the image, indicating x- and y-position.
   5. Export HSC images (*e.g.,* Multitiff-format) and perform edge detection (*e.g.,* using Matlab build-in function 'edge') to define the stagnation point location at each time step i (x_i and y_i).
   6. Subtract the position of the surface (step 5.1.5) from the position of the spectrometer probing location(s) (step 5.1.4) for each time step to obtain their distances $d(t)$ from the surface.

2. Emission spectra processing (all post-processing can for instance be performed within Matlab).
   1. Export all recorded spectrum files (wavelength vs. intensity) and calibrate the intensity response of each recorded spectrum by:
   $S_{exp,cal} = (S_{exp} - S_{bg}) / \tau_{exp} \times C$,
   with the experimentally obtained spectrum S_{exp}, the background file S_{bg} (step 3.4.2), the experimental integration time τ_{exp} and the calibration factor C determined during step 4.2.1.
   2. If several spectrometers are used, assess the validity of the calibration coefficient C using the freestream spectra taken during step 3.9. Plot all calibrated free-stream spectra together; their responses should be nearly identical because the spectrometer collection volumes in the plasma flow are very close to each other.
   3. Open the file containing the wavelength vector of the calibrated spectra (*e.g.,* double-click the .mat file in MATLAB) and identify the row indices corresponding to wavelengths $\lambda_1 = 370$ nm and $\lambda_2 = 390$ nm (alternatively, use the "find" command in Matlab).
   Note: For pyrolyzing ablators phenol originated species are also available, such as C_2, CH, H, NH, OH.
   4. Integrate the emission signal of interest (here CN violet emission, 370-390 nm) between the two indices (λ_1 and λ_2) from step 5.2.3 for each time step ($I_{\lambda 1 - \lambda 2}(t)$).
   5. Plot with software of choice the spectrally integrated emission ($I_{\lambda 1 - \lambda 2}(t)$) of each spectrometer (step 5.2.4) as a function of the spectrometer distances from the surface (step 5.1.6) (**Figure 2**) (For example, plot(d(:,1:3),I(:,1:3),'x')).
   6. For better interpretation of the results, perform a polynomial fit of the data and plot the results (*e.g.,* using MATLAB's polyfit command:
   [p,ErrorEst] = polyfit(d(:,1:3),I(:,1:3),9);
   [fit,delta] = polyval(p,d(:,1:3),ErrorEst); plot(d,fit))
   Note: Depending on the location and resolution of the recorded spectra, the excited states temperature of molecules can be determined. Use a radiation simulation tool to fit numerical spectra to experimental spectra of the CN violet and C_2 swan systems. Several online tools include spectral fitting tools to obtain translational, rotational, vibrational, and electronic temperatures[30].

6. Post-test Sample Inspection

1. Scanning Electron Microscopy (SEM) to study the carbon fibers & char layer degradation
   Note: Due to their high electrical conductivity, no further treatment is necessary in the case of fully charred carbon samples. Charging and distortion of the images will occur if virgin phenolic resin is present within the test sample.
   1. If possible, place the full test sample in the vacuum chamber of the SEM device to examine the char layer avoiding any destruction of the surface.
   Note: A detailed description of SEM and X-Ray Microanalysis applied to composite materials is given in literature[31] and not included in this protocol.
   2. Use a virgin (not tested) material sample as reference to study the carbon fiber dimensions:
      1. Select one single, well observable fiber with the SEM system.
      2. Estimate the virgin carbon fiber thickness and fiber length with the tools provided by the SEM system software according to manufacturer's instructions. For example, search in the toolbar for "Measurement" and select "Ruler", then tap the beginning and end points of the target object (*e.g.,* the start and end points of a single fiber).

Note: This produces a connecting line segment and the distance is displayed. Successively conduct this operation as necessary.

3. Identify the fiber degradation mechanisms on the tested sample, for instance a needle shape, suggests an oxygen diffusion-limited ablation regime[28], whereas pitting of the fibers and local attacks might be due to a reaction controlled regime and/or local active sites due to impurities of the material.
4. Cut the brittle material using a scalpel. Investigate the in-depth degradation and estimate the depth in which the fibers are thinned by comparing the thickness of ablated fibers to the virgin fiber thickness (step 6.1.2.2).
5. Detect possible soot formation and carbon deposition at the surface on pyrolyzing ablators, this can be enhanced if the sample was tested in an oxygen-poor atmosphere (*e.g.*, nitrogen or argon).
6. Use Energy-dispersive X-ray analysis (EDX)[31] along with the SEM to detect and identify impurities of the material that may lead to increased reactivity (*e.g.,* calcium and potassium).

Representative Results

The openly available bulk material was a highly porous carbon-bonded carbon fiber preform (CBCF), consisting of a short fiber insulation originating from rayon (cellulose fiber made from purified cellulose). The chopped, discontinuous virgin carbon fibers are interconnected in a matrix produced by the carbonization of phenolic resin. During this process the fibers become oriented and the microstructure and properties are anisotropic. The material is then vacuum-treated at temperatures above 2,300 K to ensure its temperature stability and the absence of outgassing. The material was machined in-house to hemispherical (HS) test samples of radius 25 mm with 50 mm in length. The samples have an initial density of about 180 kg/m^3 with an initial porosity of 90%.

The VKI Plasmatron facility has been used for all the experiments for the reproduction of the aero-thermodynamic environment of re-entry plasma flows, creating a high-enthalpy, highly dissociated subsonic gas flow. The gas is heated by induction through a coil, creating a high purity plasma flow. An overview of the test chamber and a schematic of the experimental instrumentation for *in-situ* ablation measurements can be found in **Fig. 1(a)** and **1(b)**. Experimental test conditions and overall results, such as averaged recession rate obtained from HSC imaging and mass loss are listed in **Table 1**. We used a two-color pyrometer, employing a wide (0.75-1.1 µm) and narrow (0.95-1.1 µm) spectral band for the temperature determination at 1 Hz acquisition rate (1,300-3,300 K). Using two narrow wavelength bands and under the assumption of an emissivity being independent of the wavelength, the surface temperature can be estimated without knowledge of its emissivity. The pyrometer was pointed and focused in the stagnation area of the sample through a 1 cm thick quartz window, at an angle of 35° with respect to the stagnation line. The instrument was calibrated up to 3,300 K by a black body source.

The surface recession was measured by the HSC with a resolution of 0.2 mm. It is evident that caliper rule recession measurements generally resulted in larger values than those performed by HSC imaging, with a difference in total recession between the two methods ranging from 0.45 to 0.9 mm. The highest uncertainty for this measurement was introduced by compressing the brittle char layer with the caliper rule. Recession rates in air varied between 44.6 and 58.4 µm/sec. It is furthermore apparent that HSC-determined recession rates in air plasma did not differ much, probably due to a diffusion-controlled ablation regime. In this regime, the surface temperature is high enough to cause complete consumption of the available oxygen at the surface, and consequently, ablation is restricted by the diffusion of oxygen through the boundary layer[32,33]. Conversely, in an oxidation reaction controlled environment, oxygen diffuses faster through a boundary layer than it is consumed at the surface and ablation increases with surface temperature. Recession rates of the CBCF material in high-enthalpy environments are also reported by MacDonald *et al*. (56 µm/sec)[22] and Löhle *et al*. (50 µm/sec)[34]. Those values lie between our measurements, although MacDonald *et al*. used a cylindrical test sample shape and Löhle *et al*. a test sample embedded in a water-cooled probe.

Three low-resolution spectrometers were used for observation of the gas-phase. Advantage of this instrument is a fast scanning of a wide spectral range (200 - 1,000 nm) that allows for detection of multiple molecules and atoms, present in ablation analysis.

Integrated CN emission intensities, plotted over distance from the ablating surface show very good agreement with respect to each other (**Fig. 2**). The data are labeled according to their respective positions from the sample surface with 'close', 'middle', and 'far'. The three spectrometers measured the same CN violet emission intensity once the fixed optical path collected light from the same distance in front of the surface. The integrated intensities of all three spectrometers almost coincide 3.4 mm before the ablating surface. Both cases show that the recorded CN violet emission peaked just in front of the test sample, before decreasing through the boundary layer. From those results we deduce that the material burn-off in air during the whole test time was very stable, and that the recorded emission signal dropped about 90% within 5 mm frontal of the surface. CN violet experimental spectra were then used for comparison to simulated spectra in order to obtain gas temperatures. The synthetic spectra were obtained using SPECAIR 2.2, assuming a Boltzmann distribution of excited levels and a least-squares fitting procedure was applied to estimate translational-rotational temperatures T_{rot} and vibrational-electronic temperatures T_{vib} (**Fig. 3**). Two conditions, at low (a) and high (b) pressure are presented, with the spectra taken close to the wall in the boundary layer. The estimated temperatures yielded a high deviation from thermal equilibrium at low pressure (**Fig. 3(a)**). The same analysis was performed for several distances from the surface, better illustrating the deviation from thermal equilibrium close to the wall at low pressure (**Fig. 4(a)**, 15 hPa), equilibrating through the boundary layer. The retrieved temperatures were in the order of 8,200 K for T_{rot} and 21,000 K for T_{vib} close to the wall, with T_{vib} decreasing towards 8,200 K through the boundary layer. This is in contrast to the equilibrium condition throughout the boundary layer at higher pressure (**Fig. 4(b)**, 200 hPa). The temperature bounds were based on an uncertainty of 10% on the spectrometer emission intensity, allowing a theoretical spectrum variation within those limits for the fitting procedure.

At low pressure, excitation transfer between molecules is reduced due to fewer collisions, which may explain the equilibrating effect towards the boundary layer edge. We assume a strong influence of molecular nitrogen at low plasma enthalpies on CN production, followed by vibrational excitation of CN. Dissociative adsorption of highly vibrationally excited nitrogen is assumed to create reactive sites at the surface that lead to CN production. Boubert and Vervisch describe this process in a nitrogen/carbon-dioxide plasma at low pressure[35]. This process may create a pool of nitrogen atoms at the surface, with exothermic reactions leading to excess energy being converted into rotational and vibrational excitation of CN.

Micrographs proved that carbon oxidation in air plasma led to an icicle shape of the ablated fibers with an oxidation depth of around 0.2 mm (**Fig. 5(a)**). This kind of icicle shaping due to ablation is widely reported in literature for carbon-carbon composite materials[36-38]. The icicle shape (opening angle) depends on the reaction-diffusion competition at the surface of the porous material, and hence, varies with oxygen diffusion. This length is assumed to correspond to the average depth of oxygen diffusion. The icicle shape additionally confirms diffusion-controlled ablation. In contrast, reaction limited ablation would allow oxygen to float into the deeper fiber structure, producing local pitting of the carbon fibers.

Bright sparking was observed during some ablation tests (**Fig. 5(b)**), which might be caused by hot fiber clusters detaching from the surface. Ablation in nitrogen plasma led to highly degraded fibers along their surface, which led to a slow recession of the material by nitridation (**Fig. 5(c)**). As the reactivity of carbon to nitrogen is much lower than that to oxygen, nitrogen is able to diffuse deeper into the material, leading to degradation along the whole fiber.
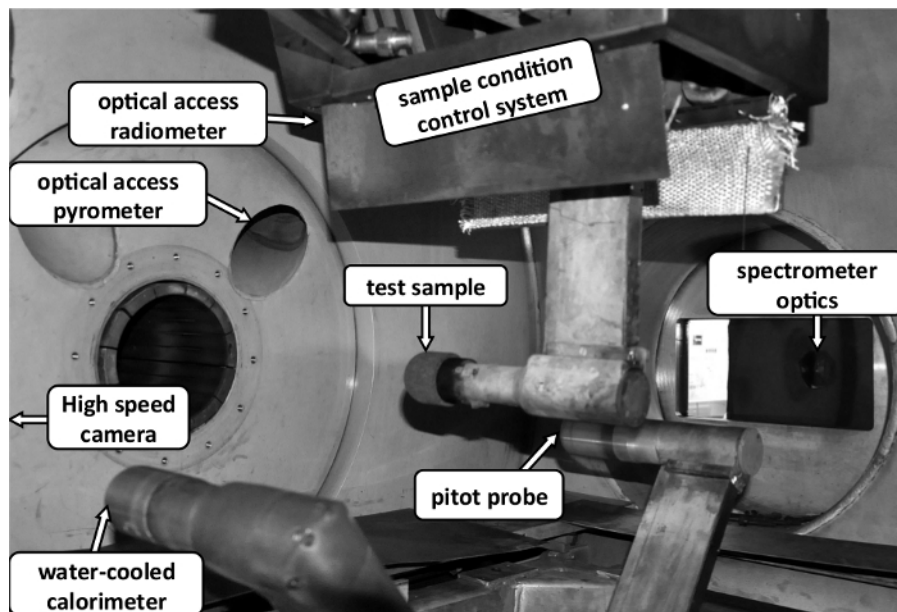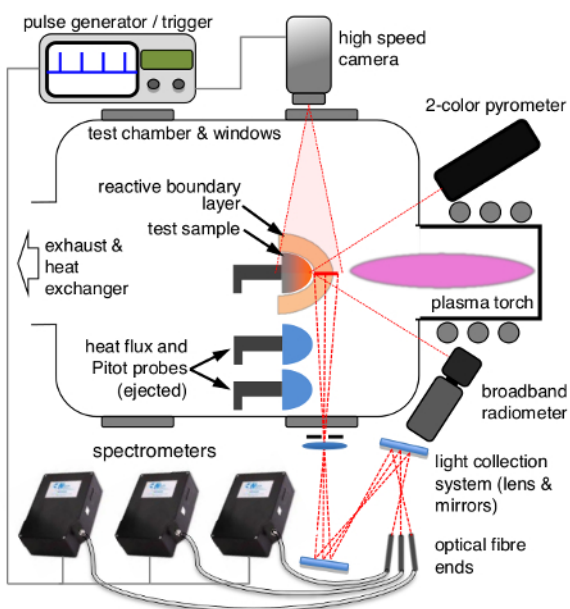
Figure 1. Plasmatron and experimental setup overview. (**a**) VKI Plasmatron test chamber overview indicating test sample outside the retention system, heat flux and pressure probes, and optical accesses for radiometers, HSC, and spectrometer optics. (**b**) Schematic of the experimental setup. Please click here to view a larger version of this figure.

Tag[a]	Gas	p_s [kPa]	p_d [Pa]	P [kW]	q_{cw} [kW/m²]	t [s]	T_s [K]	r/t [µm/s] Caliper[b]	r/t [µm/s] HSC	$\Delta m/t$ [mg/s]
A1a	Air	1.5	141	166	1019	91	2125	58.2 ± 1.7	47.8 ± 0.3	48.2
A1b	Air	1.5	342	365	3074	30.7	2750	68.3 ± 0.6	46.3 ± 4.5	69.8
A2a	Air	20	–	188	1050	91.2	1977	50.4 ± 1.7	44.6 ± 1.4	53.2
A2b	Air	20	48	321	2962	30.8	2675	84.3 ± 0.6	58.4 ± 1.4	74.6
N1a	N₂	1.5	124	154	1057	90.7	1985	3.31 ± 1.7	0	3.47
N1b	N₂	1.5	285	350	3149	31.2	2550	9.61 ± 0.6	6.85 ± 8.42	8.42

[a] A: air plasma, N: nitrogen plasma

[b] Precision: ±0.05 mm, but compression/destruction of char layer can lead to higher measurement uncertainty.

Table 1. Plasmatron test conditions and experimental results of carbon preform samples. Test case reference, test gas, static pressure p_s, dynamic pressure p_d, generator power P, mean cold wall heat flux q_{cw}, test sample exposure time τ, mean surface temperature T_s, recession rate r/τ, and mass loss rate m/τ.
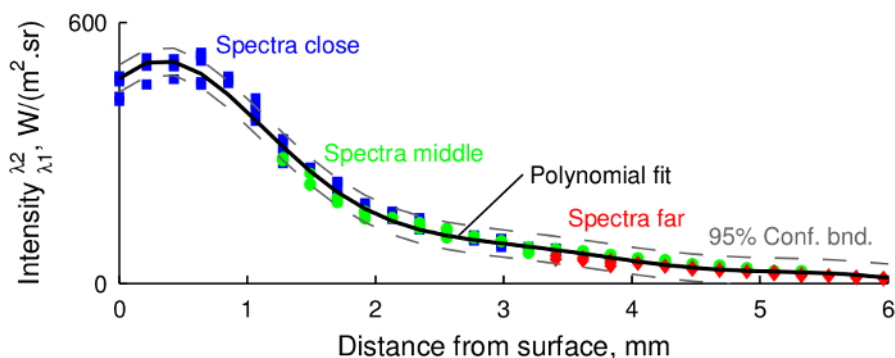

Figure 2. Spatial CN violet emission in boundary layer. Emission profiles recorded by three adjacent spectrometers during preform ablation in air coincide well when the fixed optical paths were collecting light from the same distance in front of the ablating surface: stable material burn-off, and reactive boundary layer size ~5 mm frontal of the surface (condition A1a). Please click here to view a larger version of this figure.
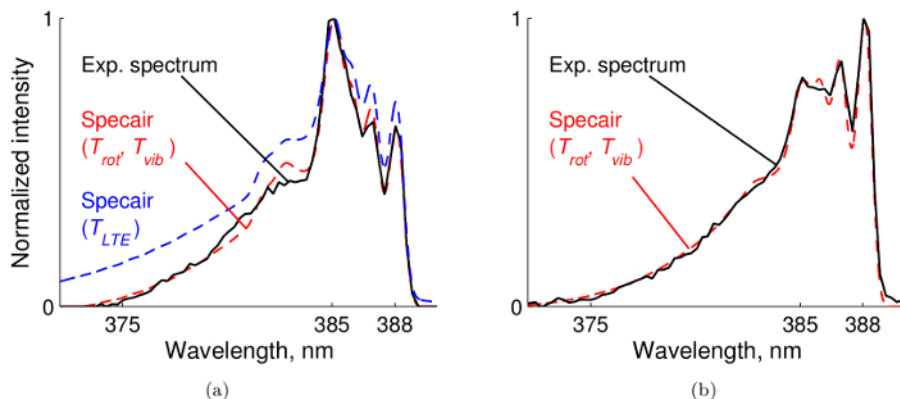

Figure 3. CN violet temperatures estimated from spectral fitting method. Least-squares method for best fitting of CN violet spectra computed with SPECAIR 2.2 provided translational-rotational and vibrational-electronic temperatures T_{rot} and T_{vib}: (**a**) Condition A1a: T_{rot} = 8,240 K ± 400 K, T_{vib} = 21,600 K ± 1,700 K, T_{LTE} = 12,600 K ± 500 K (equilibrium simulation T_{LTE} indicated for comparison); (**b**) Condition A1a: T_{rot} = 6,880 K ± 200 K, T_{vib} = 7,120 K ± 180 K. Please click here to view a larger version of this figure.
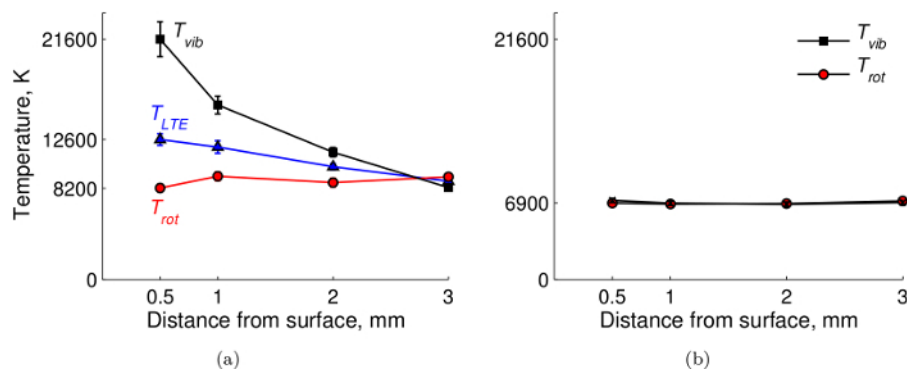
Figure 4. CN violet temperature profiles in boundary layer. Translational-rotational and vibrational-electronic temperatures T_{rot} and T_{vib} from simulated, fitted CN violet spectra computed with a radiation simulation tool at four distances from the ablating surface suggest deviation from a thermal equilibrium condition close to the wall at a low pressure of 15 hPa (**a**) but present equilibrium throughout the boundary layer at 200 hPa (**b**). The temperature bounds [K] were based on an uncertainty of 10% on the spectrometer emission intensity, allowing a theoretical spectrum variation within those limits for the fitting procedure. Please click here to view a larger version of this figure.
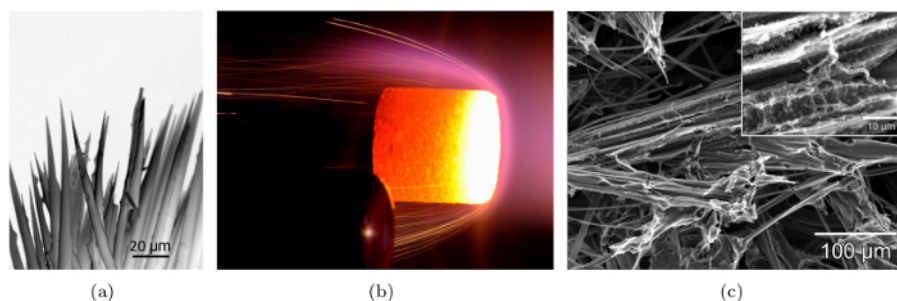

Figure 5. Scanning Electron Micrographs after air ablation (a), including *in-situ* photograph (b) and micrographs after nitrogen ablation (c). (**a**) Post air-ablation micrographs taken at frontal surface close to stagnation point present thinning of carbon fibers due to oxidation from fiber tip, leading to icicle shape, the depth of oxygen diffusion is close to 200 μm (diffusion limited ablation); (**b**) Photograph taken during ablation test of a cylindrical test sample (exposure time: 1/200 sec) illustrates bright sparking; (**c**) Strong corrosion was observed in nitrogen along whole fiber length. Please click here to view a larger version of this figure.

Discussion

This protocol describes procedures for the material characterization of reacting thermal protection materials in high enthalpy flows and presents sample results obtained on a non-pyrolyzing, ablating carbon-bonded carbon fiber (CBCF) precursor. The CBCF material is very similar to the rigid precursor for low-density carbon-phenolic ablators such as PICA and Asterm, which are the ultimate targets of the presented techniques. The main advantages of the CBCF material are its low price and open availability, since it is not restricted to export control licenses. It was chosen for presentation of the authors' approach as other research institutions can easily obtain raw CBCF material. With this publication, the authors envisage the definition of a relatively straightforward standard procedure, facilitating comparison with other laboratories.

The core techniques are a non-intrusive method to track the material recession and probing of the chemistry in the reactive boundary layer by emission spectroscopy. Application of high-speed imaging is a straightforward technique but care has to be taken with alignment of the camera system and the expected surface radiance. A short exposure time in the order of few microseconds helps to avoid saturation of the camera sensor.

A few photogrammetric techniques for ablator recession are reported in the literature, for example by Löhle et al.[34]. They are superior to our technique due to imaging of the whole ablator surface at higher resolution. The authors state a resolution of 21 μm, which is almost one order of magnitude higher than that of the technique presented in our work. However, installation of the photogrammetric setup, calibration, and post-processing are time consuming (the authors report 1 day/test), and two optical ports are required if two independent cameras have to be used. Test campaigns that require a high number of test samples make this application very costly. The technique presented in this protocol is easily set up and post-processing can be done with existing numerical tools. Our technique met the target objective of following the surface recession *in situ*. The accuracy of our technique could be further increased with a higher camera resolution or higher focal length of the optical system. However, if the material analysis requires high spatial resolution of surface details, we suggest the employment of photogrammetric techniques.

Care has to be taken with the alignment and calibration of the optical system for optical emission spectroscopy (OES). This technique is limited to line-of-sight measurements and the probing is constrained to electronically excited atoms and molecules. But its simplicity and high return on investment still governs over more elaborate techniques such as for example laser-induced fluorescence (LIF) spectroscopy, which is difficult to carry out near the surface during ablation analysis. Although LIF spectroscopy has successfully been applied to the investigation of ground state species populations in the plasma freestream[39,40], LIF measurements in the boundary layer are relatively rare. Measurements of SiO in front of a hot SiC sample are reported by Feigl[41] but have not been performed yet for ablating surfaces. The receding surface of the ablator prohibits long measurement times in the boundary layer. Apart from this are LIF systems very expensive due to the high number of specific components.

The spatial and temporal evolution of ablation products is of interest for this publication, which can be relatively simply carried out by emission spectroscopy. Three low resolution, broad range spectrometers served to detect multiple atoms and molecules present during ablation testing. The optical diagnostic bench consisted of a light collecting lens, two mirrors, and one optical fiber for each of the three spectrometers. It was important for the optical setup that no light, except that focused by the lens, reached the optical fibers.

If a pyrolyzing material is being studied, numerous hydrocarbons are ejected by the material, which are omnipresent in combustion flames, such as for example Hydrogen (Balmer series, H_α and H_β), C_2 (Swan system), CH, OH, NH[42]. These can be detected with this setup. Several research groups are recently applying emission spectroscopy to analyze the reactive boundary layer forming around ablative heat shield materials[19,22,43,44]. MacDonald et al.[22] preformed ablation tests in an inductively coupled plasma. The setup consisted of a similar low-resolution spectrometer with a spectral resolution of 1.16 nm, which is lower than the resolution provided by the spectrometer used for our setup. Their initial test sample shape was a cylinder, experiencing strong edge ablation, as demonstrated by the rising surface temperature during the test. Hence, the boundary layer thermochemical condition probably changed during the experiment, complicating a time-averaged analysis. The hemispherical test sample used for our analysis did not experience edge ablation and maintained its shape during the 30 - 90 sec test time[45].

Hermann et al.[44] provide first results on radiation-ablation coupling in a magnetoplasmadynamic arcjet facility applying emission spectroscopy. This is of high interest for the scientific community as there has not been much investigation in long-duration ground-test facilities on this topic. Unfortunately, no temporal behavior of the emission in front of the pyrolyzing material is reported. Their spectra in the range 300-800 nm were concatenated to a full spectrum during post-processing from 120 nm wavelength segments, by changing the center-wavelength of the used spectrograph. Hence, several spectra were taken over time to cover the full spectral range. If the ablative material, CBCF preform and Asterm in their case, experienced a strong temporal behavior caused by both transient pyrolysis gas ejection and surface ablation, this may falsify the temporally averaged spectrum.

One advantage of the spectrograph presented in our work is thus the wide spectral range (200-900 nm) compared to slit spectrographs, which usually result in a maximum range of 120 nm at lowest resolution. The wide spectral range observed with one single acquisition allows observation of various species in the boundary layer, resulting from the ablation and pyrolysis processes, such as hydrogen containing species (OH, NH, CH, H), carbon contributors (C, CN, C_2), and contaminants (Na, Ca, K). However, if only a single species transition is of interest, a high-resolution slit-spectrograph may be applied, which further allows scanning of the full radial emission profile as was performed by Hermann et al.[44]

Applications of the experimental data are, for instance, validation of coupled CFD and material response codes. A stagnation-line code with ablative boundary condition has recently been developed at the VKI for reproduction of the flow field along the stagnation-line of spherical bodies in the VKI Plasmatron[46]. A preliminary comparison of the experimental boundary layer emission with simulated profiles was presented elsewhere[45].

The microscale analysis of tested samples was indicative of different degradation phenomena of the carbon fibers in air and nitrogen plasma. The observed icicle morphology of ablated fibers further supported the assumption of diffusion-controlled ablation, as was suggested by the nearly identical recession rates at low pressure (15 hPa). Furthermore, the absence of internal material oxidation argues against the inflow or diffusion of hot boundary layer gases into the porous test sample. Such internal oxidation, as studied numerically by Weng et al. for PICA[47], could lead to a weaker fiber structure, causing mechanical failure of the material, for example, in the form of spallation[48,49]. Therefore, we highly suggest a general microscale analysis along with high-enthalpy testing of porous carbon-composite materials for heat shield applications. The ultimate goal of a microscale analysis would be the identification of the carbon fiber intrinsic reactivities. Spatially resolved images could advance such analysis, for instance, by micro-tomography as carried out by Panerai et al.[50]. A material code was developed at the VKI using discontinuous Galerkin discretization to simulate the complex in-depth thermal response of ablative composite materials[51].This code makes use of the new thorough physico-chemical library Mutation[++], providing the thermal and transport properties of gas mixtures, including the calculation of both finite-rate gas-phase chemistry and homogeneous/heterogeneous gas/gas-solid equilibrium chemistry[52]. We envisage comparison of our experimental data to the material response code, which is able to represent the microscale state of the porous medium.

Disclosures

The authors have nothing to disclose.

Acknowledgements

References

1. Sutton, G. W. The Initial Development of Ablation Heat Protection: An Historical Perspective. *J. Spacecraft Rock.* **19** (1), 3-11 (1982).
2. Torre, L., Kenny, J. M., & Maffezzoli, A. M. Degradation behaviour of a composite material for thermal protection systems Part I - Experimental characterization. *J. Mater. Sci.* **33**, 3137-3143 (1998).
3. Duffa, G. *Ablative Thermal Protection Systems Modeling.* Amer Inst of Aeronautics. (2013).
4. Laub, B., & Venkatapathy, E. Thermal Protection System Technology and Facility Needs for Demanding Future Planetary Missions. *International Workshop on Planetary Probe Atmospheric Entry and Descent Trajectory Analysis and Science, Lisbon (Portugal).* 239-247 (2003).
5. Tran, H. K. *Development of Lightweight Ceramic Ablators and Arc Jet Test Results.* NASA. (1994).

6. Tran, H. K., *et al. Phenolic Impregnated Carbon Ablators (PICA) as Thermal Protection Systems for Discovery Missions.* NASA. (1997).
7. Ritter, H., Portela, P., Keller, K., Bouilly, J.-M., & Burnage, S. Development of a European Ablative Material for Heatshields of Sample Return Missions. *6th European Workshop on TPS and Hot structures, Stuttgart (Germany).* (2009).
8. Pulci, G., Tirillò, J., Marra, F., Fossati, F., Bartuli, C., & Valente, T. Carbon-phenolic ablative materials for re-entry space vehicles: Manufacturing and properties. *Compos: Part A.* **41**, 1483-1490 (2010).
9. Natali, M., Monti, M., Kenny, J. M., & Torre, L. A nanostructured ablative bulk molding compound: Development and characterization. *Compos: Part A.* **42**, 1197-1204 (2011).
10. Allcorn, E. K., Natali, M., & Koo, J. H. Ablation performance and characterization of thermoplastic polyurethane elastomer nanocomposites. *Compos: Part A.* **45**, 109-118 (2013).
11. Esper, J. and Lengowski, M. *Resin-Impregnated Carbon Ablator: A New Ablative Material for Hyperbolic Entry Speeds.* at <http://www.techbriefs.com/component/content/article/14610> (2012).
12. Rothermel, T. and Zuber, Ch. and Herdrich, G. and Walpot, L. A light weight ablative material for research purposes. *6th Ablation Workshop; Urbana-Champaign (US-IL).* at <http://ablation2014.engineering.uky.edu/> (2014).
13. Kendall, R. M., Bartlett, E. P., Rindal, R. A., & Moyer, C. B. *An analysis of the coupled chemically reacting boundary layer and charring ablator: Part I.* (CR 1060) (1968).
14. Milos, F. S., & Chen, Y.-K. Comprehensive model for multicomponent ablation thermochemistry. *35th Aerospace Sciences Meeting & Exhibit, Reno (US-NV).* AIAA paper 1997-0141 (1997).
15. Lachaud, J., & Mansour, N. N. Microscopic scale simulation of the ablation of fibrous materials. *48th AIAA Aerospace Sciences Meeting Including the New Horizons Forum and Aerospace Exposition, Orlando (US-FL).* AIAA paper 2010-984 (2010).
16. Lachaud, J., Cozmuta, I., & Mansour, N. N. Multiscale approach to ablation modeling of phenolic impregnated carbon ablators. *J. Spacecraft Rock.* **47** (6), 910-921 (2010).
17. Prabhu, D., *et al.* CFD Analysis Framework for Arc-Heated Flowfields, I: Stagnation Testing in Arc-jets at NASA ARC. *AIAA 2009-4080, San Antonio, TX, USA.* (2009).
18. Milos, F., & Chen, Y.-K. Ablation and Thermal Response Property Model Validation for Phenolic Impregnated Carbon Ablator. *J. Spacecraft Rock.* **47** (5), 786-805 (2010).
19. Loehle, S., Hermann, T., Zander, F., Fulge, H., & Marynowski, T. Ablation Radiation Coupling Investigation in Earth Re-entry Using Plasma Wind Tunnel Experiments. *11th AIAA/ASME Joint Thermophysics and Heat Transfer Conference, Atlanta (USA).* (AIAA 2014-2250) (2014).
20. Driver, D. M. and MacLean, M. Improved Predictions of PICA Recession in Arc Jet Shear Tests. *49th AIAA Aerospace Sciences Meeting including the New Horizons Forum and Aerospace Exposition.* AIAA paper 2011-141 (2011).
21. Uhl, J., Owens, W. P., Meyers, J. M., & Fletcher, D. G. Pyrolysis Simulation in an ICP Torch Facility. *42nd AIAA Thermophysics Conference, Honolulu (US-HI).* AIAA paper 2011-3618 (2011).
22. MacDonald, M. E. and Jacobs, C. M. and Laux, C. O. and Zander, F. and Morgan, R. Measurements of Air Plasma/Ablator Interactions in an Inductively Coupled Plasma Torch. *Journal of Thermophysics and Heat Transfer.* **29** (1), 12-23 (2015).
23. Bottin, B. *Aerothermodynamic Model of an Inductively-coupled Plasma Wind Tunnel.* Von Karman Institute for Fluid Dynamics (1999).
24. Bottin, B., Chazot, O., Carbonaro, M., van der Haegen, V., & Paris, S. The VKI Plasmatron Characteristics and Performance. *RTO AVT Course on Measurement Techniques for High Enthalpy and Plasma Flows, Rhode-Saint-Genèse (Belgium), RTO EN-8.* 6-26 (1999).
25. Guariglia, D., Helber, B., Chazot, O. Enhancement of the VKI Plasmatron Facility Capabilities for Testing High HeatFlux re-entry Conditions. *8th European Symposium on Aerothermodynamics for Space Vehicles (ESA).* (2015).
26. Kolesnikov, A. F. Conditions of Simulation of Stagnation Point Heat Transfer from a High-enthalpy Flow. *Fluid Dyn.* **28** (1), 131-137 (1993).
27. Barbante, P. F., & Chazot, O. Flight Extrapolation of Plasma Wind Tunnel Stagnation Region Flowfield. *J. Thermophys. Heat Transfer.* **20** (3), 493-499 (2006).
28. Helber, B., Chazot, O., Hubin, A., & Magin, T. Microstructure and gas-surface interaction studies of a low-density carbon-bonded carbon fiber composite in atmospheric entry plasmas. *Composites: Part A.* **72**, 96-107 (2015).
29. Svanberg, S. *Atomic and Molecular Spectroscopy.* Springer (1992).
30. *Spectralfit Specair User manual, Version 3.0.* at <http://www.specair-radiation.net/Specair manual.pdf> (2015).
31. Goldstein, J. and Newbury, D. and Joy, D. and Lyman, C. and Echlin, P. and Lifshin, E. and Sawyer, L. and Michael, J. R. *Scanning Electron Microscopy and X-Ray Microanalysis.* Kluwer Academic / Plenum Publishers, New York. (2003).
32. Scala, S. M., & Gilbert, L. M. Sublimation of Graphite at Hypersonic Speeds. *AIAA J.* **3** (9), 1635-1644 (1965).
33. Metzger, J. W., Engel, M. J., & Diaconis, N. S. Oxidation and Sublimation of Graphite in Simulated Re-entry Environments. *AIAA J.* **5** (3), 451-459 (1967).
34. Loehle, S., Staebler, T., Reimer, T., and Cefalu, A. Photogrammetric Surface Analysis of Ablation Processes in High Enthalpy Air Plasma Flow. *11th AIAA/ASME Joint Thermophysics and Heat Transfer Conference, Atlanta (US-GA).* AIAA paper 2014-2248 (2014).
35. Boubert, P., & Vervisch, P. CN spectroscopy and physico-chemistry in the boundary layer of a C/SiC tile in a low pressure nitrogen/carbon dioxide plasma flow. *J. Chem. Phys.* **112** (23), 10482-10490 (2000).
36. Lachaud, J., Aspa, Y., & Vignoles, G. L. Analytical modeling of the steady state ablation of a 3D C/C composite. *International Journal of Heat and Mass Transfer.* **51**, 2614-2627 (2008).
37. Vignoles, G. L., Lachaud, J., Aspa, Y., & Goyhénèche, J.-M. Ablation of carbon-based materials: Multiscale roughness modelling. *Compos. Sci. Technol.* **69**, 1470-1477 (2009).
38. Cho, D., and Yoon, B. I Microstructural interpretation of the effect of various matrices on the ablation properties of carbon-fiber-reinforced composites. *Composites Science and Technology.* **61**, 271-280 (2001).
39. Marynowski, T. and Löhle, S. and Fasoulas, S. Two-Photon Absorption Laser-Induced Fluorescence Investigation of CO2 Plasmas for Mars Entry. *Journal of Thermophysics and Heat Transfer.* **28** (3), 394-400 (2014).
40. Fletcher, D. Arcjet flow properties determined from laser-induced fluorescence of atomic nitrogen. *Applied Optics.* **38** (9), 1850-1858 (1999).
41. Feigl, M. and Auweter-Kurtz, M. Investigation of SiO production in front of Si-based material surfaces to determine the transition from passive to active oxidation using planar laser-induced fluorescence. *35th AIAA Thermophysics Conference.* AIAA paper 2001-3022 (2001).
42. Helber, B., Asma, C. O., Babou, Y., Hubin, A., Chazot, O., & Magin, T. E. Material response characterization of a low-density carbon composite ablator in high-enthalpy plasma flows. *J. Mater. Sci.* **49** (13), 4530-4543 (2014).
43. Wernitz, R., Eichhorn, C., Marynowski, T., & Herdrich, G. Plasma Wind Tunnel Investigation of European Ablators in Nitrogen/Methane Using Emission Spectroscopy. *International Journal of Spectroscopy.* **2013**, 1-9 (2013).

44. Hermann, T. and Loehle, S. and Leyland, P. and Marraffa, L. and Bouilly, J.-M. and Fasoulas, S. First results on ablation radiation coupling through optical emission spectroscopy from the vacuum ultraivolet to the visible. *8th European Symposium on Aerothermodynamics for Space Vehicles.* (2015).
45. Helber, B., Turchi, A., Chazot, O., Hubin, A., & Magin, T. Gas/Surface Interaction Study of Low-Density Ablators in Sub- and Supersonic Plasmas. *11th AIAA/ASME Joint Thermophysics and Heat Transfer Conference, Atlanta (USA).* AIAA paper 2014-21222 (2014).
46. Turchi, A., Helber, B., Munafò, A., & Magin, T. E. Development and Testing of an Ablation Model Based on Plasma Wind Tunnel Experiments. *11th AIAA/ASME Joint Thermophysics and Heat Transfer Conference, Atlanta (USA).* AIAA paper 2014-2125 (2014).
47. Weng, H. and Bailey, S. C. C. and Martin, A. Numerical study of iso-Q sample geometric effects on charring ablative materials. *International Journal of Heat and Mass Transfer.* **80**, 570-596 (2015).
48. Mathieu, R. D. Mechanical Spallation of Charring Ablators in Hyperthermal Environments. *AIAA Journal.* **2** (9), 1621-1627 (1964).
49. Davuluri, R. and Martin, A. Numerical study of spallation phenomenon in an arc-jet environment. *11th AIAA/ASME Joint Thermophysics and Heat Transfer Conference, Atlanta, GA (USA).* AIAA paper 2014-2249 (2014).
50. Panerai, F., Martin, A., Mansour, N. N., Sepka, S. A., & Lachaud, J. Flow-Tube Oxidation Experiments on the Carbon Preform of a Phenolic-Impregnated Carbon Ablator. *J. Thermophys. Heat Transfer.* **28** (2), 181-190 (2014).
51. Schrooyen, P. and Hillewaert, K. and Magin, T.E. and Chatelain, P. Discontinuous Galerkin discretization coupled with sharp interface method for ablative materials. *21st AIAA Computational Fluid Dynamics Conference, San Diego, CA (USA).* AIAA paper 2013-2457 (2013).
52. Scoggins, J. B., & Magin, T. E. Gibbs Function Continuation for Linearly Constrained Multiphase Equilibria. *Combust. Flame.* (2015).